



Inference of Principal Species in Caustic Aluminate Solutions Through Solid-State Spectroscopic Characterization

Journal:	<i>Dalton Transactions</i>
Manuscript ID	DT-ART-01-2020-000229.R2
Article Type:	Paper
Date Submitted by the Author:	07-Apr-2020
Complete List of Authors:	<p>Dembowski, Mateusz; Pacific Northwest National Laboratory Prange, Micah; Pacific Northwest National Laboratory Pouvreau, Maxime; Washington State University, Graham, Trenton; Pacific Northwest National Laboratory Bowden, Mark; Pacific Northwest National Laboratory N'Diaye, Alpha T. ; Lawrence Livermore National Laboratory, Advanced Light Source Schenter, Gregory; Pacific Northwest National Laboratory; Washington State University, Chemistry Clark, Sue; Pacific Northwest National Laboratory; Washington State University, Chemistry Clark, Aurora; Washington State University, Chemistry; Pacific Northwest National Laboratory Rosso, Kevin; Pacific Northwest National Laboratory Pearce, Carolyn; Pacific Northwest National Laboratory</p>

Inference of Principal Species in Caustic Aluminate Solutions Through Solid-State Spectroscopic Characterization

Mateusz Dembowski[†], Micah P. Prange[†], Maxime Pouvreau[‡], Trent R. Graham[†], Mark E. Bowden[†], Alpha N'Diaye[‡], Gregory K. Schenter^{†,‡}, Sue B. Clark^{†,‡}, Aurora E. Clark^{†,‡}, Kevin M. Rosso[†] and Carolyn I. Pearce[†]

[†]Pacific Northwest National Laboratory, Richland, Washington, 99352, United States

[‡]Department of Chemistry, Washington State University, Pullman, Washington, 99164, United States

[‡]Advanced Light Source, Lawrence Berkeley National Laboratory, Berkeley, California, 94720, United States

Abstract

Tetrahedrally coordinated aluminate $\text{Al}(\text{OH})_4^-$ and dialuminate $\text{Al}_2\text{O}(\text{OH})_6^{2-}$ anions are considered to be major species in aluminum-rich alkaline solutions. However, their relative abundance remains difficult to spectroscopically quantify due to local structure similarities and poorly understood effects arising from extent of polymerization and counter-cations. To help unravel these relationships here we report detailed characterization of three solid-phase analogues as structurally and compositionally well-defined reference materials. We successfully synthesized a cesium salt of the aluminate monomer, $\text{CsAl}(\text{OH})_4 \cdot 2\text{H}_2\text{O}$, for comparison to potassium and rubidium salts of the aluminate dimer, $\text{K}_2\text{Al}_2\text{O}(\text{OH})_6$, $\text{Rb}_2\text{Al}_2\text{O}(\text{OH})_6$. Single crystal and powder X-ray diffraction methods clearly reveal the structure and purity of these materials for which a combination of ^{27}Al MAS-NMR, Al K-edge X-ray absorption and Raman/IR spectroscopies was then used to fingerprint the two major tetrahedrally coordinated Al species. The resulting insights into the effect of Al-O-Al bridge formation, between aluminate tetrahedra on spectroscopic features may also be more general to the many materials that are based on this motif.

Introduction

In highly alkaline solutions the speciation and transformation of aluminum remain a challenge to spectroscopically interrogate, despite their centrality to a variety of major aluminum processing systems. For example, understanding how the dominant tetrahedrally-coordinated aluminate anion, $\text{Al}(\text{OH})_4^-$, transforms to octahedral aluminum (Al) during the precipitation of gibbsite, $\alpha\text{-Al}(\text{OH})_3$, is key to the efficiency of the Bayer process by which alumina, Al_2O_3 , is

extracted from bauxite ore.¹⁻³ Despite the fact that the Bayer process was invented over 120 years ago and is still used to produce nearly all of the world's Al_2O_3 supply as an intermediate step to Al production, the mechanism and kinetics of $\alpha\text{-Al}(\text{OH})_3$ precipitation have not been comprehensively described.⁴⁻⁹ Both synthetic and industrial Bayer liquors have a propensity to become supersaturated,^{10, 11} presenting a considerable engineering challenge as $\alpha\text{-Al}(\text{OH})_3$ precipitation suffers from slow kinetics and yields are poor even in the presence of seed crystals.^{12, 13} Limited mechanistic understanding of how small Al clusters of low nuclearity condense into extended sheet structures of Al octahedra in $\alpha\text{-Al}(\text{OH})_3$, or boehmite, $\text{AlO}(\text{OH})$ also directly hampers the processing of ca. 90 million gallons of highly caustic radioactive waste at U.S. Department of Energy legacy sites.^{4, 14-16} These wastes contain significant quantities of solid and solvated Al forms that originated from disposed Al-clad defense fuels and are highly caustic due to NaOH additions used to increase the lifetime of underground steel storage tanks.¹⁷

For such systems, developing the ability to spectroscopically distinguish the principal aluminum species in solution in equilibrium with $\alpha\text{-Al}(\text{OH})_3$ is critical. In sodium hydroxide, appreciable concentrations of oligomeric Al solution species relative to the aluminate monomer^{8, 9, 18} have been invoked to rationalize the propensity of these solutions to become supersaturated.^{10, 11} However, because of the predominance of tetrahedral coordination across species, spectroscopic techniques that probe the local structure around Al have limited sensitivity to oligomerization. The tetrahedrally coordinated aluminate dimer, $\text{Al}_2\text{O}(\text{OH})_6^{2-}$, has been proposed and confirmed on the basis of Raman spectroscopy.^{3, 7, 9} Ab initio molecular dynamic (AIMD) studies explored the stability and spectroscopic features of different mono- and dinuclear Al species, suggesting that $\text{Al}(\text{OH})_4^-$, $\text{Al}_2\text{O}(\text{OH})_6^{2-}$ and the dihydroxo bridged $\text{Al}_2(\text{OH})_8^{2-}$ dimer, are viable solution species under experimentally relevant conditions.¹⁹⁻²² Formation of solvent separated (SSIPs) or contact ion pairs (CIPs) with in the presence of counter cations played a significant role in stabilization of different Al species but did not affect their spectroscopic signatures.^{19, 23} Furthermore, AIMD revealed that structurally distinct, soluble Al-hydroxides can produce similar Raman and IR spectra, which has implications for data interpretation in terms of higher-order Al species. Additional experimental techniques that could quantify the species present in these caustic aluminate solutions would clearly be beneficial.

Studies on well-defined reference materials could help constrain the spectroscopic signatures of the monomer, dimer, and higher extents of polymerization. Crystalline hydroxide salts of aluminate have proven useful in both regards but remain an underexploited platform. For example, the assignment of solution Raman signals required the isolation and characterization of the solid phase $\text{Al}_2\text{O}(\text{OH})_6^{2-}$ unit, which was possible in the KOH system by precipitation of $\text{K}_2\text{Al}_2\text{O}(\text{OH})_6$.^{3, 24} Specifically, under experimental conditions where $[\text{OH}^-] = 8.0 \text{ M}$, and $[\text{Al}^{3+}] = 3.0 \text{ M}$, substitution of NaOH with KOH, or CsOH led to change in the percentage contribution of bands associated with the $\text{Al}_2\text{O}(\text{OH})_6^{2-}$ species (as a function of total Raman signal) from 32, to 29, and 24%, respectively.⁷ And because it was demonstrated that the identity of the cation (e.g. Na^+ , K^+ , or Cs^+) has real, but minor effect on the equilibrium between the $\text{Al}(\text{OH})_4^-$ and the products of its oligomerization, comparison across systems containing other alkali cations can be informative.¹⁻³ Despite these advantages this approach has received limited attention to date.^{5, 25}

Here, we explore the principle aluminate species present in caustic aluminate solutions by precipitating solid phases from supersaturated KOH, RbOH, and CsOH solutions and employing multi-modal solid phase characterization to resolve the bonding environment around the Al atom. For the first time, the monomeric cesium aluminate hydroxy hydrate salt, $\text{CsAl}(\text{OH})_4 \cdot 2\text{H}_2\text{O}$, was isolated from solution, and shown by single crystal X-ray diffraction (XRD) to exhibit unusually short ...O...O interactions between the terminal hydroxide O atoms and that of the water molecule. The tetrahedral dimers, $\text{K}_2\text{Al}_2\text{O}(\text{OH})_6$ and $\text{Rb}_2\text{Al}_2\text{O}(\text{OH})_6$ were crystallized, and high-resolution crystal structures were obtained. The Raman, infrared, nuclear magnetic resonance and X-ray absorption spectroscopic signatures for these monomeric and dimeric structures that represent the dominant Al species in concentrated caustic aluminate solutions were obtained and, where possible, compared with those predicted by AIMD simulations. This detailed description of monomeric and dimeric aluminate species is also relevant to the chemical building blocks of Al-containing minerals, transition aluminas, and zeolites.^{26, 27}

Experimental

Synthesis of alkali aluminates

$\text{K}_2\text{Al}_2\text{O}(\text{OH})_6$ (1). A modified version of the procedure reported in the literature was used to synthesize **1**.²⁴ Inside of a N_2 filled glovebox, 30 mL Teflon bottle was charged with 3.49 g (62 mmol) of KOH (Fisher Scientific, $\geq 85.0\%$) and 4.00 g of H_2O (18 $\text{M}\Omega\text{-cm}$). The resulting mixture was equilibrated to room temperature, then 1.00 g (37 mmol) of Al wire (Sigma-Aldrich, 99.999%) was added in ca. 100 mg equivalents over a period of three days. At the end of reaction, the resulting white solid was separated by centrifugation (8000 RPM for 10 min) and the clear, colorless solution was filtered through a 0.2 μm syringe filter (Whatman). The resulting solution was capped and stored at 25°C under N_2 . Diffraction quality crystals resulted in two weeks. Bulk material was collected using vacuum filtration and was washed five times with absolute ethanol (Fisher Scientific, ACS grade)

$\text{Rb}_2\text{Al}_2\text{O}(\text{OH})_6$ (2). The same procedure for **1** was used to synthesize **2** but 7.47 g (62 mmol) of $\text{RbOH}\cdot\text{H}_2\text{O}$ (Strem Chemicals, 99.8%) was added instead of instead of KOH.

$\text{CsAl}(\text{OH})_4\cdot 2\text{H}_2\text{O}$ (3). The synthesis procedure for **3** was the same as **1** but 10.41 g (62 mmol) of $\text{CsOH}\cdot\text{H}_2\text{O}$ (Acros Organics, 99.95%) was added instead of KOH.

Single crystal X-ray diffraction. Diffraction quality crystals were isolated and mounted on a cryoloop in oil. Data was collected on a Bruker Venture equipped with Ag $\text{K}\alpha$ X-radiation microfocus source ($\lambda = 0.5609 \text{ \AA}$). Data collections were performed under a stream of nitrogen gas, affording a temperature of 110 K. Bruker APEX III software package was used to correct the data for Lorentz, polarization, and background effects. Empirical absorption corrections were performed using the SADABS software package.²⁸ SHELXTL was used for structure solution and refinement.^{29, 30} The structure of $\text{CsAl}(\text{OH})_4\cdot 2\text{H}_2\text{O}$ (**3**) was refined as an inversion twin with a ratio of 0.77:0.33. H-atoms were located in structures **1** and **2** from diffraction maps and refined using the DFIX d s command ($d = 0.96$ and $s = 0.01$). No H-atoms could be located in the structure of **3**. All non H-atoms were refined anisotropically.

Powder X-ray diffraction (PXRD) patterns were collected using a Rigaku D-Max II microbeam diffractometer and a rotating Cr anode source ($\lambda = 2.2910 \text{ \AA}$). The powders were loaded into boron-glass capillaries (Charles Supper, MA) and sealed with wax. The incident beam was collimated to 300 μm diameter and diffracted intensities recorded on a large image plate which were converted to powder profiles using the Rigaku 2D-Max software. The measured PXRD

patterns were compared with patterns calculated from the crystal structures using TOPAS v6 (Bruker AXS).

Raman spectroscopy was carried out using a Horiba LabRam HR spectrometer in the 100-4000 cm^{-1} spectral region using a 633 nm continuous light source and a 40x optical objective mounted on a Nikon Ti-E inverted microscope. Ten spectra were collected with 30 second exposure times and then averaged. Peak deconvolution and integration, including linear background correction in the 550-700 cm^{-1} region, was accomplished using the Multipeak Fitting 2 package as implemented in IgorPro 8 software. The peak deconvolution routine used three Voigt profiles to fit the signals observed at 614, 621, and 647 cm^{-1} in the spectrum of **3**.

Infrared spectroscopy was carried out using a Bruker Tensor 37 spectrometer with a DTGS detector and air-cooled source. Spectra were collected using an attenuated total reflectance accessory with a diamond/KRS5 internal reflection element with nine reflections (SensIR Technologies). For each sample, a total of 128 spectra were collected and averaged, using a wavenumber range of 600 to 4000 cm^{-1} , and with a resolution of 4 cm^{-1} .

^{27}Al magic angle spinning nuclear magnetic resonance spectroscopy was carried out at 20°C using an 850 MHz Varian-DDR (19.975 T, ^{27}Al Larmor frequency of 221.413 MHz) NMR spectrometer, with a commercial 1.6 mm pencil-type MAS probe and a rotor spinning rate of 20 kHz. The parameters used to acquire NMR spectra for quantitative analysis were sweep width of 833.33 kHz, recycle delay of 1 s, (an array of recycle delay time from 0.5 to 5 s confirmed recycle delay of 1 s as sufficient for reaching equilibrium state), acquisition time of 20 ms, 256 transients, and a small tip angle $\pi/20$ (corresponding to pulse width of 0.55 μs). Chemical shifts were externally referenced to 1 M $\text{Al}(\text{NO}_3)_3$ (in H_2O) at 0 ppm. Isotropic chemical shift (δ_{iso}), quadrupolar coupling constant (C_Q), and asymmetry parameter (η_Q) were estimated using *sola* peak fitting procedure and *QUAD all* model as implemented in TopSpin (v4.0.5).

Al K-edge X-ray absorption near edge structure (XANES) and extended X-ray absorption fine structure (EXAFS) spectroscopy measurements were performed at the Advanced Light Source (Berkeley, CA) at beamline 6.3.1. The samples were mounted in a N_2 filled glovebox by pressing the powder into indium foil to secure the sample and minimize charging. The indium foil was then attached to a Cu metal sample holder using silver paint, and the holder was maintained in

a N₂ atmosphere until it was loaded into the beamline endstation. A reference spectrum collected on corundum (α -Al₂O₃) was used to calibrate the energy scale.³¹ The X-ray absorption spectra were collected under vacuum at room temperature in total electron yield (TEY) mode over the scan range from 1520 to 1850 eV. Al K-edge XANES and EXAFS data were background corrected and analyzed using the Athena and Artemis interfaces to the IFEFFIT program.³²

Ab initio molecular dynamics. To analyze the Al K-edge EXAFS, FEFF calculations were performed on ensembles of structures drawn from DFT molecular dynamics (MD) trajectories with the Quickstep module of the CP2K software.³³ The DFT functional consisted of a revised version of the PBE functional³⁴ with the empirical dispersion corrections of Grimme et al.³⁵ Within the mixed gaussian and plane waves scheme³³ a double-zeta basis set was used with a single set of polarization functions,³⁶ Goedecker-Teter-Hutter pseudopotentials together with plane wave cutoffs of 600 to 900 Ry depending on the hardness of the pseudopotentials. Starting from the experimental coordinates, hydrogen atoms were added to the relevant oxygen atoms. To account for the dispersion interactions and reach convergence in the relaxed cell dimensions normalized to the unit cell, supercells of factors $1 \times 2 \times 1$ for K₂Al₂O(OH)₆ and Rb₂Al₂O(OH)₆, and $2 \times 2 \times 2$ for CsAl(OH)₄·2H₂O, were created. With a timestep of 0.5 fs, *NPT*-ensemble MD was performed for 20 ps and *NVT*-ensemble MD was performed with equilibration and production stages of respectively 5 ps and 20 to 35 ps, using the average lattice dimensions of the last 10 ps of the *NPT* run.

Results and Discussion

Crystal structures of K, Rb, and Cs aluminates

Table 1. Crystallographic Data for Unit Cells of $\text{Al}(\text{OH})_4^-$, and $\text{Al}_2\text{O}(\text{OH})_6^{2-}$

compound	1	2	3
empirical formula	$\text{K}_2\text{Al}_2\text{O}(\text{OH})_6$	$\text{Rb}_2\text{Al}_2\text{O}(\text{OH})_6$	$\text{CsAl}(\text{OH})_4 \cdot 2\text{H}_2\text{O}$
molecular weight ($\text{g} \cdot \text{mol}^{-1}$)	250.20	342.95	263.95
crystal system	Orthorhombic	Orthorhombic	Monoclinic
space group	<i>Aba2</i>	<i>Aba2</i>	<i>C2</i>
<i>a</i> [Å]	10.1605(12)	10.3511(8)	10.4124(15)
<i>b</i> [Å]	7.5416(8)	7.6823(7)	6.6986(10)
<i>c</i> [Å]	9.9990(12)	10.2481(8)	6.2156(10)
α [°]	90	90	90
β [°]	90	90	126.129(4)
γ [°]	90	90	90
<i>V</i> [Å ³]	766.19(15)	814.93(12)	350.16(9)
<i>Z</i>	4	4	2
R_1/wR_2 [for $I > 2\sigma(I)$]	0.0367	0.0426	0.0274
R_1/wR_2 [for all data]	0.0503	0.0791	0.0786
GOF	1.122	1.070	1.205
Largest diff. peak/hole [$\text{e} \cdot \text{Å}^{-3}$]	0.463/-0.530	1.135/-1.494	0.937/-1.025

The aluminate dimers, $\text{K}_2\text{Al}_2\text{O}(\text{OH})_6$ (**1**), and $\text{Rb}_2\text{Al}_2\text{O}(\text{OH})_6$ (**2**) are isostructural and crystallize in orthorhombic *Aba2* (space group no. 41) unit cells. Although the structure of **1** has been previously reported, that of the **2** was only inferred from powder X-ray diffraction studies.³⁷ To promote direct comparison, and to improve upon the quality of the previously reported structure of the $\text{K}_2\text{Al}_2\text{O}(\text{OH})_6$, a higher-resolution structure was obtained. The aluminate dimer structure consists of two symmetry-related, tetrahedrally-coordinated Al centers bridged via a μ_2 -O bridge with Al-O-Al angles of 133.26° and 136.20°, and O-Al-Al-O torsion angles of 41.13° and 34.27°, for **1** and **2** respectively (**Figure 1**, bottom). The Al centers are further coordinated by three hydroxide groups with Al-OH distances ranging from 1.761(2) to 1.779(2) Å for **1**, and 1.761(3) to 1.781(3) Å for **2**. The Al- μ_2 -O bond distance in **1** (1.7177(15) Å) is comparable to the corresponding Al- μ_2 -O bond in **2** (1.7203(18) Å).

The Cs aluminate monomer, $\text{CsAl}(\text{OH})_4 \cdot 2\text{H}_2\text{O}$ (**3**) crystallizes in a monoclinic *C2* (space group no. 5) unit cell. The structure of **3** consists of an Al center coordinated by four hydroxide groups resulting in tetrahedral geometry and Al-OH distances ranging from 1.747(15) to

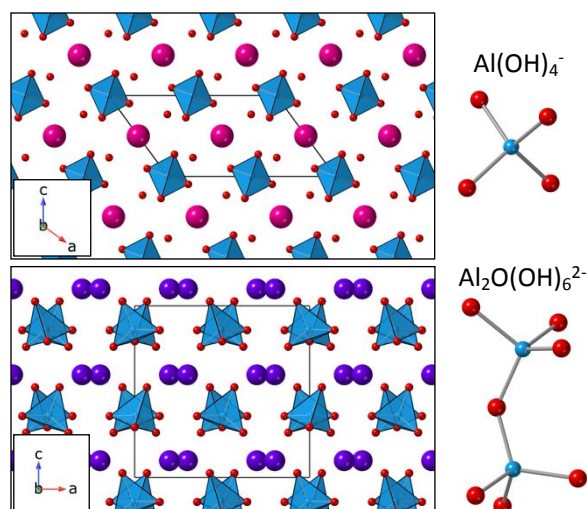


Figure 1. Polyhedral view down 0 1 0 direction (left) and ball-and-stick (right) representation of the Al(OH)_4^- (top) and $\text{Al}_2\text{O(OH)}_6^{2-}$ (bottom) structures. Blue polyhedra and spheres represent aluminum. Red, magenta, and purple spheres represent oxygen, cesium, and potassium (or rubidium), respectively. H-atoms are omitted for clarity.

1.756(14) Å (**Figure 1**, top). While the synthesis conditions used to produce **1**, **2**, and **3** are similar (see **Experimental Section**), the dimeric species crystallize as anhydrous salts while the monomeric unit is a dihydrate. The water molecules in **3** are related by symmetry and located within a tetrahedral cavity defined by Cs atoms and coordinated via two strong (2.253 and 2.557 Å) and two weak (2.896 and 3.147 Å) H-bonds to hydroxide ligands of the four neighboring aluminate ions (**Figure 2**). Efforts to determine the positions of H-atoms in the structure of **3** were unsuccessful. Difficulty in determining the H-atom positions are likely caused by the fact that the difference-Fourier maps are dominated by scattering from heavy Cs atoms ($Z = 55$) and/or positional disorder of the light H-atoms ($Z = 1$). Generally, the Al-O distances observed in the structures of **1-3** are consistent with prior literature reports for tetrahedrally coordinated Al species.^{38, 39}

The unusually short distance between the oxygen atom present in the Al(OH)_4^- unit and the neighboring water molecule ($\text{O}\cdots\text{O}_d - 2.253\text{Å}$) indicates the presence of a nearly symmetrical H-bond reminiscent of the Zundel-ion, H_3O_2^- .⁴⁰⁻⁴² Prior studies reported comparable $\text{O}\cdots\text{O}_d$ in various structures featuring H_3O_2^- ions.⁴³⁻⁴⁵ For example, H_3O_2^- present in the unit cell of $\text{Na}_2[\text{Et}_3\text{MeN}][\text{Cr}(\text{PhC}(\text{S})\text{N}(\text{O}))_3] \cdot \frac{1}{2}\text{NaH}_3\text{O}_2 \cdot 18\text{H}_2\text{O}$ exhibits $\text{O}\cdots\text{O}_d$ of 2.29 Å while the $\text{O}\cdots\text{O}_d$ in the structure of $[\text{Mo}_3\text{O}_2(\text{O}_2\text{C}_2\text{H}_5)_6(\text{H}_2\text{O})_2](\text{H}_3\text{O}_2)\text{Br}_3 \cdot 6\text{H}_2\text{O}$ was 2.52 Å.^{46, 47} In these studies, the $\text{O}\cdots\text{O}_d$

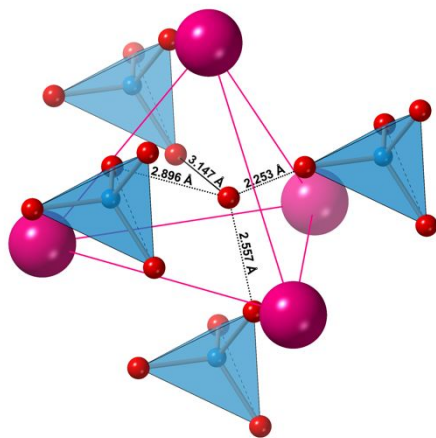


Figure 2. Polyhedral and ball representation of the H_2O environment in the structure of $\text{CsAl}(\text{OH})_4 \cdot 2\text{H}_2\text{O}$ (**3**). Black dotted lines represent H_2O -OH interactions. H-atom positions were not determined experimentally. Blue polyhedra and spheres represent aluminum. Magenta and red spheres represent cesium and oxygen, respectively.

elongated significantly (2.41-2.54 Å) when the H_3O_2^- moiety acted as a bridging ligand between metal ions in polynuclear complexes.⁴⁸ In addition to inorganic and organometallic complexes, short $\text{O} \cdots \text{O}_d$ distances have been a topic of studies in mineralogy,^{49, 50} biological systems,^{51, 52} dense polymorphs of ice,^{53, 54} and during the proton transfer reactions in aqueous solutions.^{42, 55}

The synthesis products **1-3** were characterized using powder X-ray diffraction (PXRD). Experimental and simulated diffraction patterns are shown in **Figure 3**. The results show good agreement with calculated patterns derived from single crystal X-ray diffraction experiments (see above). Minor variations between observed and predicted intensities were attributed to preferential orientation of the relatively large crystallites (ca. 50-100 μm) precluding analysis via Rietveld refinement. In addition, variable intensities occur in micro-diffraction experiments when

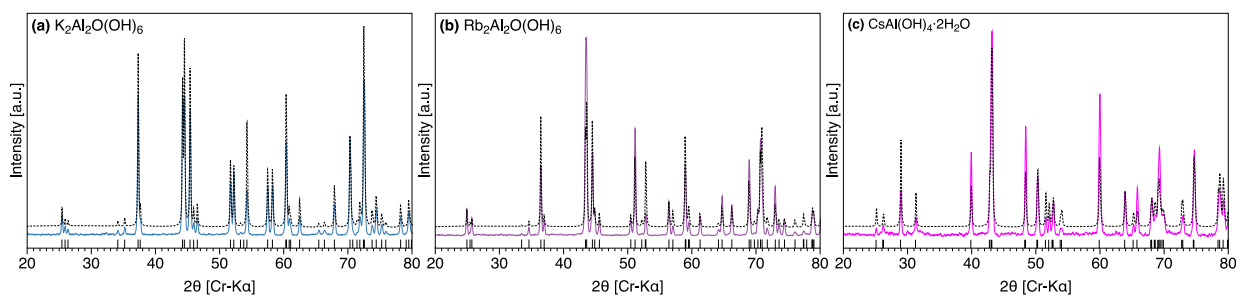


Figure 3. Experimental (color traces) and calculated (black dashed traces) powder X-ray diffraction patterns for bulk **1** (a), **2** (b), and **3** (c). Calculated spectra are offset vertically for clarity.

there are insufficient crystallites in the collimated beam to give statistically averaged intensities over all orientations.

²⁷Al MAS-NMR Spectroscopy

The quadrupolar nature of the ²⁷Al nucleus ($I = 5/2$) provides a powerful tool for evaluation of the local symmetry about the Al center due to the interactions of the nuclear quadrupole moment with the local electric field gradients.⁵⁶ To minimize second order quadrupole interactions and to obtain the best approximation of the isotropic chemical shift (δ_{iso}), quadrupole coupling constant (C_Q), and asymmetry parameter (η_Q), a high-field (850 MHz, 19.975 T) NMR instrument was used. In accordance with single crystal X-ray diffraction results all ²⁷Al MAS-NMR spectra were fit using a single Al site. Comparisons of experimental and modeled spectra, including spinning side-band manifold, and difference spectra are summarized in **Figure 4**, **S1**, and **S2**. Two weak resonances are noted at ca. 10 and 15 ppm and are marked with an

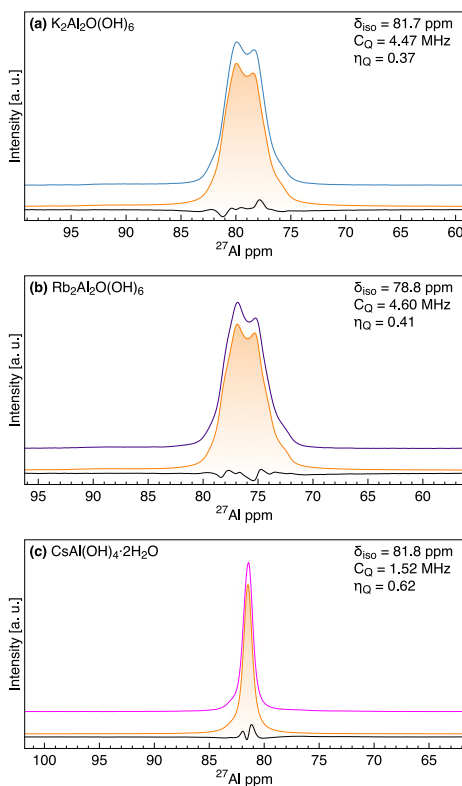


Figure 4. Experimental ²⁷Al MAS-NMR of **1** (top, blue trace), **2** (middle, purple trace), and **3** (bottom, magenta trace) collected at 19.975 T and 20 kHz spin rate. Model fits are presented in orange and offset horizontally for clarity. Difference spectra are shown in black.

asterisk (**Figure S2**). The relative intensity of these resonances changes randomly from sample **1** to **3** indicating presence of more than one species. Peak integration reveals that the impurity account for ca. 3.9% of the total Al in the sample of **1**, 2.8% of **2**, and 4.7% of **3**. The relative position of these resonances indicates octahedral coordination.⁵⁶ Thus, sample purity of $\geq 95\%$ was confirmed by both XRD and ^{27}Al MAS-NMR, accounting for the potential presence of crystalline and amorphous impurities.

^{27}Al Chemical shifts of **1-3** obtained from the fitting procedure fall between 78.8 and 81.8 ppm. Resonances in this chemical shift region are consistent with tetrahedral geometry observed in single crystal X-ray diffraction measurements.^{56, 57} Direct comparison of the chemical shift observed for the monomeric (**3**) and dimeric species (**1-2**) is difficult due to the complex effect of cations on isotropic chemical shifts (δ_{iso}). For instance, the two dimeric systems (K at 81.7 ppm vs. Rb at 78.8 ppm) show a 2.9 ppm disparity in their δ_{iso} despite their isostructural nature. A similar variation arises when the chemical shift of **3** ($\delta_{\text{iso}} = 81.8$ ppm) is compared to that of $\text{Na}_2[\text{Al}(\text{OH})_4]\text{Cl}$ ($\delta_{\text{iso}} = 86.6$ ppm) resulting in a 5.0 ppm difference.⁵⁸ Presence of highly electronegative element ($\chi_{\text{Cl}} = 3.16$) in the proximity of NMR active nuclei contributes to a downfield shift in the δ_{iso} . Similarly, recent AIMD calculations demonstrated that the relative position of the Na atom, with respect to Al, can influence the ^{27}Al chemical shift with shorter $\text{Al}\dots\text{Na}_d$ distances leading to more downfield chemical shifts.⁶ The $\text{Al}\dots\text{Na}_d$ in $\text{Na}_2[\text{Al}(\text{OH})_4]\text{Cl}$ is 3.675 Å while the $\text{Al}\dots\text{Cs}_d$ in **3** is 4.207 Å. Consequently, it is unclear if the presence of chloride in the structure and/or shorter $\text{Al}\dots\text{M}_d^+$ in $\text{Na}_2[\text{Al}(\text{OH})_4]\text{Cl}$ led to the observed chemical shift. Generally, the influence of the cation on the ^{27}Al chemical shift was demonstrated in a number of prior solution studies at high hydroxide concentration where presence of Na^+ led to an upfield chemical shift, as compared to K^+ .^{18, 59} Further studies implementing isostructural complexes are necessary to establish similar chemical shift relationships in the solid-state.

Quadrupole coupling constants (C_Q) and asymmetry parameters (η_Q) estimated from the fitting procedure for **1** ($C_Q = 4.47$ MHz, $\eta_Q = 0.37$) compare favorably with prior literature reports at $C_Q = 4.42$ MHz and $\eta_Q = 0.21$.⁶⁰ Small differences in C_Q observed between **1** and **2** ($\Delta = 0.13$ MHz) likely arise from distortions of the $\text{Al}_2\text{O}(\text{OH})_6^{2-}$ unit in the form of Al-O-O-Al torsion angle (41.13° for **1**, and 34.27° for **2**) resulting in a more eclipsed conformation of the $-\text{Al}(\text{OH})_3$ terminal

units in **2** (**Figure S3**). The C_Q and η_Q parameters obtained for **3** can be compared to those of the tetrahedral Al site present in γ - Al_{13} Keggin. Note: the $\text{Na}_2[\text{Al}(\text{OH})_4]\text{Cl}$ study did not report C_Q or η_Q parameters.⁵⁸ Despite the fact that **3** and γ - Al_{13} Keggin contain isolated $(\text{Al}(\text{OH})_4)$ and fully polymerized (AlO_4) polyhedra, respectively, the symmetry about the Al centers is approximately T_d as compared to C_{3v} in the case of **1** and **2**. The C_Q (1.52 MHz) and η_Q (0.62) for **3** are analogous to these observed in γ - Al_{13} ($C_Q = 1.75$ MHz, $\eta_Q = 0.85$)⁶¹ suggesting that presence of H-atoms in **3**, which can lead to decrease of the overall symmetry of $\text{Al}(\text{OH})_4^-$, have minimal impact on the interactions of the nuclear quadrupole moment. Furthermore, the non-zero value of the C_Q determined for **3** indicates a small degree of asymmetry that is consistent with the determined crystal structure (**Figure 2**). Specifically, the presence of a very strong H-bonds, and two unique Al-O distances in the $\text{Al}(\text{OH})_4^-$ unit, result in perturbation of the idealized T_d symmetry that is reflected in ^{27}Al NMR measurements. Collectively, ^{27}Al MAS-NMR results demonstrate that formation of Al-O-Al bridges in AlO_4 polyhedra leads to significant spectroscopic changes that can be leveraged in studies of more complex systems dominated by tetrahedrally coordinated Al.

X-ray Absorption Spectroscopy

Local symmetry and bonding environments about Al centers present in the structures of **1-3** were further probed using Al K-edge X-ray absorption spectroscopy (XAS). Al-K edge X-ray absorption near edge structure (XANES) spectra of $\text{K}_2\text{Al}_2\text{O}(\text{OH})_6$ (**1**), $\text{Rb}_2\text{Al}_2\text{O}(\text{OH})_6$ (**2**), and $\text{CsAl}(\text{OH})_4 \cdot \text{H}_2\text{O}$ (**3**) are shown in **Figure 5**. The XANES spectrum of **1** yields two edge maxima at 1566.2 eV (*i*) and 1569.2 eV (*ii*) and a single ill-defined feature at 1582.2 eV (*iii*). The XANES spectrum of **2** similarly yields two edge maxima at 1565.5 eV (*i*) and 1568.9 eV (*ii*) and a feature at 1580.7 eV (*iii*). The position of the edge maxima in the spectra of **1** and **2** compare favorably with literature values for tetrahedrally coordinated Al ranging from ca. 1565 to 1567 eV for feature (*i*) and 1570 to 1573 eV for feature (*ii*).³¹ The origin of these features is attributed to the excitation from Al 1s to a mixture of O 3p and Al 3p states of the tetrahedrally coordinated Al centers present in the structures of **1** and **2**.^{39, 62} The shift of the edge maxima to higher energy observed for **1** when compared to **2** is consistent with prior FEFF calculations relating shorter Al-O bond lengths to positive shift in energy.⁶³ The broad, ill-defined features observed at ca.

1580 eV in the spectra of **1** and **2** are characteristic of tetrahedrally coordinated Al and arise due to multiple scattering in the first coordination shell of Al oxides.^{38, 64}

The spectrum of **3** yields a single, broad edge maximum at 1568.6 eV (*ii*) and a feature at 1581.7 eV (*iii*). The position of the edge maximum in the spectrum of **3** is anomalously high approaching values expected from six-coordinate Al centers with typical edge maxima at ca. 1568 eV. It is worth noting that maxima observed at this energy have also been reported as corresponding to tetrahedral Al present in zeolites.⁶⁵ The relatively small energy difference between tetrahedral and octahedral Al (ca. 2 eV), paired with structural diversity of previously studied materials leads to uncertainty in assignment of the coordination number of **3**.⁶⁶ However, the extensive characterization discussed above, and presence of the 1581.7 eV feature in the XANES spectrum of **3** indicate that the 1568.6 eV edge maximum correspond to tetrahedrally coordinated Al.

To the extent possible, Al K-edge extended X-ray absorption fine structure (EXAFS) spectroscopy was used to determine the bond distances and coordination number of the scattering atoms. However, Al K-edge (1559 eV) falls in the “tender” energy range of 1 to 5 KeV, which has unique experimental limitations including a decrease in X-ray flux across the energy range associated with the beamline design, a limit in the volume sample and difficulties in data analysis are a result of significant multiple scattering contributions from ligands at close distances. In addition, the presence of Si in the beam path (Si K-edge – 1839 eV)³⁹ necessitated truncation of the EXAFS data (**Figure 6**, top). To circumvent the experimentally imposed limitations, FEFF⁶⁷ calculations were performed on ensembles of structures drawn from ab initio

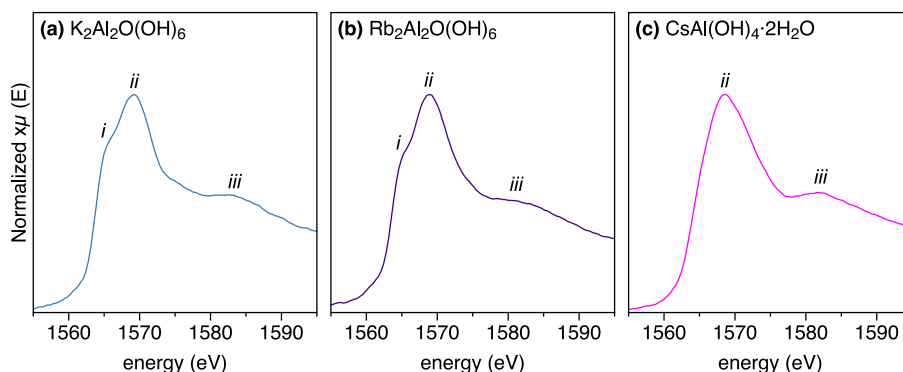


Figure 5. Comparison of experimental (blue, purple, and magenta traces) Al K-edge XANES spectra of **1-3** with three tetrahedral features indicated with *i-iii*.

molecular dynamics (AIMD) trajectories. The AIMD EXAFS were evaluated against experimental EXAFS data for **1**, and the subsequent AIMD-derived EXAFS spectra for **1-3** were used to evaluate the sensitivity of this technique to isolated versus polymerized AlO_4 units.

The AIMD-derived EXAFS spectrum (weighted by k^3) for **1** and its Fourier transform are compared to the experimental data in **Figure 6**. Agreement between AIMD-derived data and experimental data is good, with the only adjustable parameter being E_0 (adjusted via the EXCHANGE card) – no bond lengths or thermal disorder (Debye-Waller) factor adjustments were made, and the amplitude reduction factor, S_0^2 , was left at its default value of 1.0. In fact the FEFF defaults were found to be appropriate for all parameters, and a comprehensive list of cards in the feff input file used is: RPATH 6, EXAFS 15, POTENTIALS and ATOMS cards describing one sampled structure from AIMD trajectory. FEFF was then run for each structure in the ensemble, and the results were averaged. With the 6 angstrom cutoff, the FEFF pathfinder yielded between 139 and 189 scattering paths for each ensemble structure. The EXAFS is dominated by single scattering from the nearest-neighbor O atoms, giving a sinusoidal signal (single-scattering and

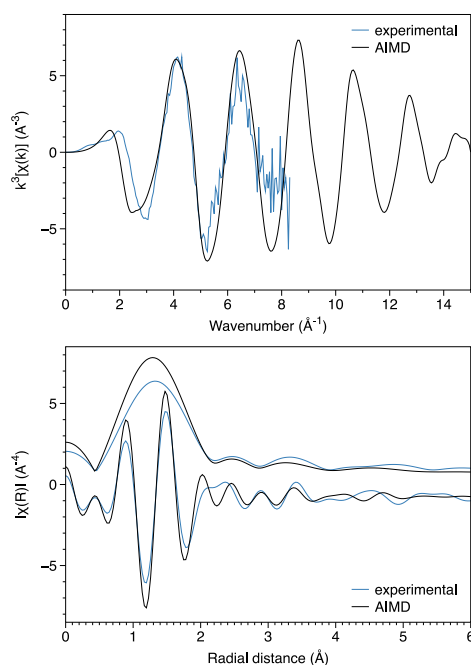


Figure 6. (top) comparison of experimental and predicted EXAFS region in k -space for **1**. (bottom) experimental (solid blue trace) and predicted (black trace) EXAFS of **1** in R -space showing magnitude and real component. k -range used for forward Fourier transform: 3 to 7 \AA^{-1} .

first-shell only simulations for a fixed structure are compared in the supporting information). The slight mismatch in the frequency of the main sinusoid (visible as a displacement of the theoretical first-shell peak in the R-space plot in **Figure 6**) can be attributed to errors in the first shell distance (single-scattering half path length). But the sign of this error is surprising, since the average Al-O distance from the scXRD measurements described above is 1.755 Å while the average Al-O distance in the MD trajectory is 1.778 Å (suggesting that the AIMD first shell peak should be at larger, not smaller, R). The overestimation of the EXAFS amplitude in the AIMD can be attributed to insufficient disorder in the model (which contains simulated thermal motion in a 136-atom cell that is periodically repeated), relative to the actual structure, and to broadening of the experimental signal as energy above the edge is increased.

Evaluating the predicted EXAFS spectra for **1-3** (**Figure 7a**) in k-space reveals a systematic variation of the amplitudes ($\text{Cs} > \text{Rb} > \text{K}$). The relative thermal motion of the cations likely accounts for the observed discrepancies with the K^+ system having larger amplitude due to its smaller mass. Specifically, calculated thermal displacement parameters (including static and thermal disorder) for the Al-O single scattering path are $\sigma^2 = 0.0023, 0.0020,$ and 0.0017 \AA^2 for

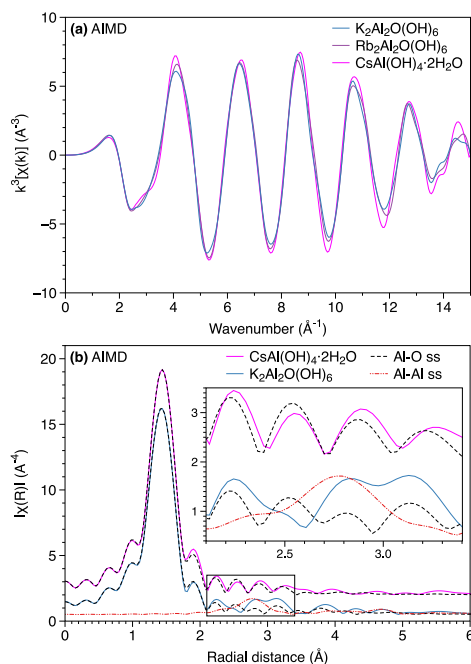


Figure 7. (a) comparison of the AIMD predicted EXAFS for **1**, **2**, and **3** in k-space. (b) R-space EXAFS showing magnitude for **1** and **3**. k-range between 3 and 13 \AA^{-1} used for forward Fourier transform.

1, **2**, and **3**, respectively. A forward Fourier transform of the AIMD predicted EXAFS data for **1** and **3** was performed in the k -range 3 and 13 \AA^{-1} , and the spectra in R -space are shown in **Figure 7b**, together with contributions from Al-O (**1**, **3**) and Al-Al (**1**) single scattering (ss) paths. The EXAFS features arise primarily from Al-O ss paths, and the presence of Al-O-Al bridges can be inferred from the complex features observed between ca. 2 and 3.5 \AA . **Figure 7b** (inset) highlights the spectral region where constructive, and destructive interference between the Al-O and Al-Al ss paths in **1** give rise to complex features that are distinct from those observed in **3**. Furthermore, contributions of Al-O ss paths are similar in **1** and **3** despite measurable differences in Al-O bond lengths and presence of an additional Al-O ss path in the structure of **3** due to the presence of a water molecule. The same feature arising due to Al-Al and Al-O ss path interactions is noted in the predicted EXAFS of **2** (**Figure S4**). These results suggest that, if experimental data can be obtained out to a k of 13 \AA^{-1} , Al K-edge EXAFS can be used to distinguish between isolated and polymerized AlO_4 units.

Raman and IR Spectroscopy

Solid-state Raman and IR spectra obtained from aluminate salts (**1-3**) are shown in **Figure 8**. Raman spectra of K, and Rb aluminate dimers (**1,2**) exhibit three distinct bands in the Al-O(H) stretching region located at 548, 688, and 726 cm^{-1} for the K salt, and at 543, 685, and 725 cm^{-1} for the Rb salt. Bands at ca. 545 cm^{-1} were previously assigned to the symmetric vibration of the Al-O-Al unit while those at ca. 685 and 725 cm^{-1} to the vibrations of the $-\text{Al}(\text{OH})_3$ units and Al-O-H bending modes.^{3, 19, 20}

The O-H stretching region exhibits three distinct bands at 3259, 3378, and 3551 cm^{-1} for **1** and 3327, 3387, and 3572 cm^{-1} for **2**. Presence of three hydroxide stretches in the spectra of aluminate dimers is consistent with the presence of three crystallographically unique oxygen atoms comprising the $-\text{Al}(\text{OH})_3$ unit. Examination of the structure of **1** reveals all three terminal hydroxides acting as H-bond donors, and two as H-bond acceptors (**Figure 9**). Specifically, O1 accepts one H-bond (O-H...O, 1.860 \AA), while O2 accepts two (1.889 and 2.171 \AA). Acting as an H-bond acceptor results in weakening of the O-H covalent bond and a shift in the corresponding stretching frequency to lower wavenumbers.⁶⁸ Consequently, the peaks at 3259, 3378, and 3551 cm^{-1} for **1** are assigned to the stretching of the O2(H), O1(H), and O3(H) groups, respectively.

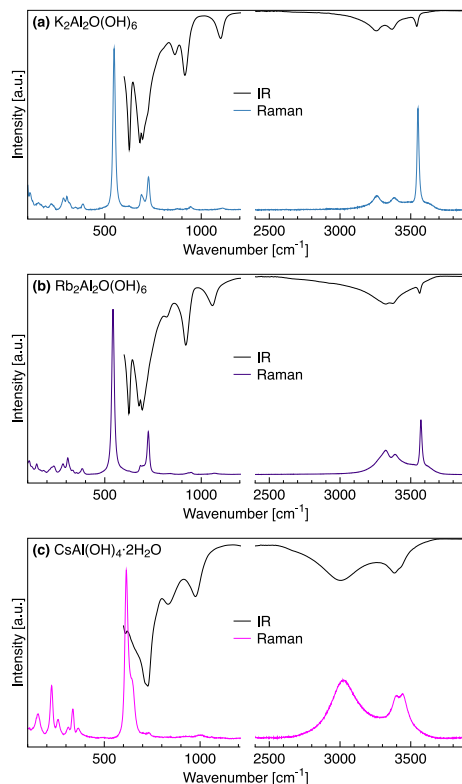


Figure 8. Solid-state Raman (colored) and IR (black) spectra of the **1** (top), **2** (center), and **3** (bottom).

Analogous breakdown of the bonding environment in **2** results in assignment of Raman signals at 3327, 3387, and 3572 cm^{-1} to the stretching of the O1(H), O3(H), and O2(H) groups, respectively.

The IR spectra of **1** and **2** exhibit five distinct bands in the Al-O(H) stretching region at 627, 681, 696, 864, and 912 cm^{-1} for **1**, and at 625, 679, 694, 820, and 917 cm^{-1} for **2**. Bands at ca. 625 cm^{-1} correspond to the asymmetric vibrations of the Al-O-Al units while those at ca. 680, 695, and 915 cm^{-1} to the vibrations of the $-\text{Al}(\text{OH})_3$ units. The 864/1101 cm^{-1} (**1**) and 820/1055 cm^{-1} (**2**) bands correspond to the Al-O-H bending modes.^{3, 19} Bands at 3253, 3363, 3542 cm^{-1} for **1** and 3316, 3370, and 3561 cm^{-1} for **2** correspond to vibrations of the three unique hydroxide groups (see above).

Raman spectrum of **3** exhibits three overlapping bands in the Al-O stretching region located at 614, 621, and 647 cm^{-1} (**Figure 10**). An additional weak signal is noted at ca. 731 cm^{-1} . In prior computational studies evaluating the monomeric $\text{Al}(\text{OH})_4^-$ moiety, a singular Raman active band was predicted in this region, corresponding to the symmetric vibration of the AlO_4

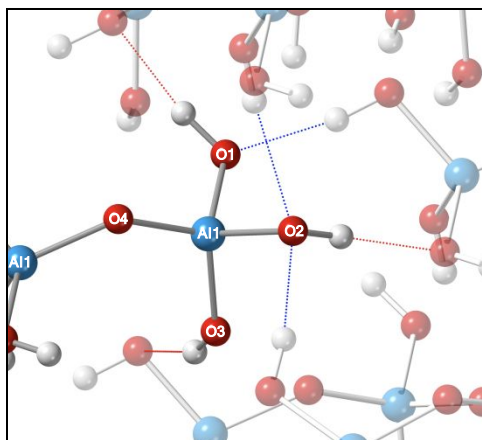


Figure 9. Ball-and-stick representation of the bonding around the $\text{Al}_2\text{O}(\text{OH})_6^{2-}$ in **1**. Blue, and red dotted lines represent accepted and donated H-bonds respectively. Light blue, red, and white spheres represent aluminum, oxygen, and hydrogen, respectively.

unit.^{19, 20} The difference between the symmetric and asymmetric vibration of the AlO_4 unit was predicted to be ca. 97 cm^{-1} , therefore the emergence of additional bands at ca. 620 cm^{-1} cannot be attributed to activation of the asymmetric vibration.¹⁹ The weak intensity and position of the band at ca. 731 cm^{-1} , however, is consistent with activation of the asymmetric vibration of the AlO_4 unit. Consequently, all three bands observed between 610 and 650 cm^{-1} likely correspond to the symmetric vibration of the AlO_4 unit. We propose that the observed splitting arises due to i) perturbation of the idealized T_d symmetry, ii) asymmetry of the $\text{Al}(\text{OH})_4^-$ local environment (**Figure 10**, right), iii) presence of unusually strong O-H...H-OH interactions, iv) crystal packing effects (e.g. Davydov splitting)⁶⁹ or a combination of these.

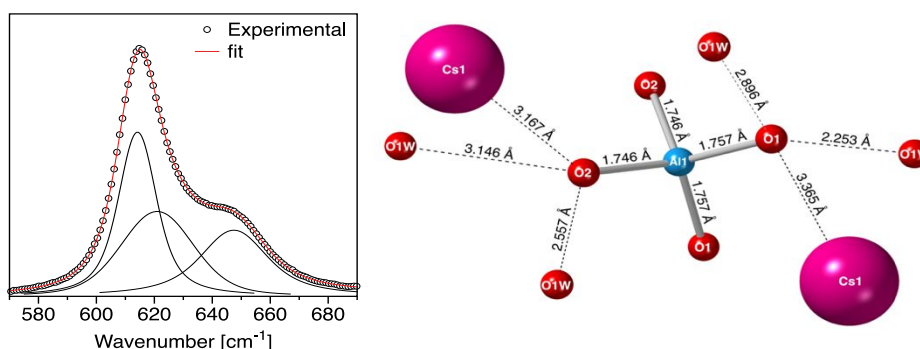


Figure 10. (left) deconvolution of the Raman spectra showing the ν_1 symmetrical stretching region of the $\text{CsAl}(\text{OH})_4 \cdot 2\text{H}_2\text{O}$ (**3**) and (right) ball-and-stick representation of the local symmetry around O1 and O2 in the structure of **3**. Environments of symmetry related atoms (O1 and O2) are omitted for clarity. Blue, red, and magenta spheres represent aluminum, oxygen, and cesium, respectively.

The O-H stretching region in Raman spectrum of **3** shows three distinct bands at 3025, 3395, and 3443 cm^{-1} . Although it was possible to determine the position of H-atoms in the structure of **1** and **2**, efforts to assign specific positions to H-atoms in the structure of **3** were unsuccessful, and the proposed assignments are tentative. The bands observed at 3395, and 3443 cm^{-1} are assigned to the O-H stretching vibrations of two unique OH groups present on the $\text{Al}(\text{OH})_4^-$ unit and that at 3025 cm^{-1} to the O-H stretching vibrations of the singular crystallographically unique water molecule. The broad nature of the latter band indicates possible disorder in H-atom positions that might explain the difficulty in their crystallographic refinement. It is worth noting that the position of the O-H stretching of the H_2O molecule is shifted to lower wavenumbers compared to those noted in a number of ice polymorphs.^{54, 70} This is in accordance with the short O...O distance observed in the structure of **3**.

The IR spectrum of **3** shows bands at 607, 709, and 827 cm^{-1} in the Al-O(H) stretching region. On the basis of its weak intensity and position, the band at 607 cm^{-1} is assigned to the activation of the symmetric vibration of the AlO_4 unit while that at 709 cm^{-1} to its asymmetric vibration.^{19, 20} Notably, the strong band at 709 cm^{-1} shows significant asymmetry with shoulders appearing at both lower, and higher wavenumbers (ca. 659 and 727 cm^{-1}) that likely arise due to the splitting of AlO_4 vibrations described above. The origin of the band at 827 cm^{-1} is unclear as no bands are expected in this spectral region on the basis of AIMD predictions.¹⁹ Prior studies focusing on the symmetrization of H-bonds in ice noted emergence of a vibration at ca. 900 cm^{-1} assigned to the O-O vibrational mode.^{40, 71} However, lack of a corresponding signal in the Raman spectrum (**Figure 8**) makes the assignment of this band ambiguous. The band at 972 cm^{-1} in the IR spectrum of **3** is assigned to the bending mode of the Al-O-H. The band at 3004 cm^{-1} is assigned to the vibration of the unique water molecule while those at 3376 and 3428 cm^{-1} to two unique O-H groups present in $\text{Al}(\text{OH})_4^-$ moiety.

The Raman and IR spectra obtained for the mono- (**3**) and dimeric (**1-2**) aluminate species show distinct sets of signals in the Al-O, and O-H stretching region making them powerful tools in discerning these species. Although prior solution studies utilized the Al-O spectral region to evaluate Al speciation, that corresponding to O-H stretching was rarely evaluated.⁸

Conclusions

Expanding studies of caustic aluminate solutions from Na systems to systems containing K, Rb, and Cs resulted in isolation, in the solid state, of the aluminate monomer, $\text{Al}(\text{OH})_4^-$, and the aluminate dimer, $\text{Al}_2\text{O}(\text{OH})_6^{2-}$. Crystal structures determined by single crystal X-ray diffraction defined the positions of H-atoms in $\text{Al}_2\text{O}(\text{OH})_6^{2-}$ and revealed an unusually short O...O bond distance in the Cs aluminate monomer. A combination of single crystal and powder X-ray diffraction demonstrated that these materials were of sufficiently high purity ($\geq 95\%$) to be used for subsequent spectroscopic characterization.

Multi-modal spectroscopic techniques used to evaluate the different salts of $\text{Al}(\text{OH})_4^-$ and $\text{Al}_2\text{O}(\text{OH})_6^{2-}$ established a set of spectroscopic features that can be used to evaluate tetrahedrally coordinated Al in more complex environments. The change in the symmetry about the tetrahedrally coordinated Al center, caused by the formation of the Al-O-Al bridge in the K and Rb dimers, is reflected in a significant increase in the ^{27}Al MAS-NMR quadrupole coupling constant, C_Q . From this result, it can be surmised that the presence of two, or three Al-O(H)-Al bridges in AlO_4 tetrahedra will lead to significantly higher C_Q values ($\gg 1.5$ MHz). Comparison of the asymmetry parameter, η_Q , and C_Q of $\text{CsAl}(\text{OH})_4 \cdot 2\text{H}_2\text{O}$ and $\gamma\text{-Al}_{13}$ revealed that presence of H-atoms in the second coordination sphere of Al has a minimal effect on the interactions of the nuclear quadrupole moment.

Furthermore, Al K-edge X-ray absorption spectroscopy was also established as an efficient tool to distinguish between the mono- and dimeric forms of anionic aluminate. XANES spectra of dimeric aluminate anion shows two distinct edge maxima as opposed to a single feature observed in the monomeric aluminate anion.

Implementation of AIMD to evaluate the potential of EXAFS spectroscopy to distinguishing between different forms of the aluminate anions revealed weak but real contributions from the Al-Al single scattering paths that allow for their effective disambiguation. IR and Raman spectroscopy of tetrahedrally coordinated mono- and dinuclear aluminates show unique, non-overlapping signatures in the Al-O, and O-H spectral regions. Comparison of spectra obtained from $\text{Al}_2\text{O}(\text{OH})_6^{2-}$ as a K^+ , and Rb^+ salt reveal that the identity of the cation has a

relatively small effect ($< 5 \text{ cm}^{-1}$) on the Al-O stretching region and a stronger effect ($< 68 \text{ cm}^{-1}$) on the O-H stretching region.

The spectroscopic signatures of two fundamental Al units – $\text{Al}(\text{OH})_4^-$ and $\text{Al}_2\text{O}(\text{OH})_6^{2-}$ were hereby established. Comparison of their spectroscopic signatures from the perspective of structural differences and oligomerization may help advance understanding of aluminum speciation and transformations in the highly alkaline solutions found in the Bayer process and in the processing of U.S. Department of Energy legacy nuclear wastes. The structure-property relationships may also help advance fundamental understanding of catalytic processes occurring on related materials such as zeolites or activated aluminas.

Acknowledgements

This research was supported as part of IDREAM (Interfacial Dynamics in Radioactive Environments and Materials), an Energy Frontier Research Center funded by the U.S. Department of Energy (DOE) Office of Science, Basic Energy Sciences (BES). X-ray absorption spectroscopy data were collected at the Advanced Light Source, which is a DOE Office of Science User Facility under Contract DE-AC02-105CH11231. XRD, Raman, IR and NMR spectroscopy data were collected using the William R. Wiley Environmental Molecular Sciences Laboratory (EMSL, grid.436923.9), a national scientific user facility sponsored by the DOE's Office of Biological and Environmental Research located at Pacific Northwest National Laboratory (PNNL) under proposal number 49771. PNNL is a multiprogram national laboratory operated for DOE by Battelle Memorial Institute under Contract No. DE-AC05-76RL0-1830.

References

- (1) Hind, A. R.; Bhargava, S. K.; Grocott, S. C., The Surface Chemistry of Bayer Process Solids: A Review. *Colloids Surf. A* **1999**, *146*, 359-374.
- (2) Smith, P., The Processing of High Silica Bauxites - Review of Existing and Potential Processes. *Hydrometallurgy* **2009**, *98*, 162-176.
- (3) Moolenaar, R. J.; Evans, J. C.; Mckeever, L. D., Structure of Aluminate Ion in Solutions at High pH. *J. Phys. Chem.* **1970**, *74*, 3629-3636.
- (4) Peterson, R. A.; Buck, E. C.; Chun, J.; Daniel, R. C.; Herting, D. L.; Ilton, E. S.; Lumetta, G. J.; Clark, S. B., Review of the Scientific Understanding of Radioactive Waste at the US DOE Hanford Site. *Environ. Sci. Technol* **2018**, *52*, 381-396.
- (5) Graham, T. R.; Han, K. S.; Dembowski, M.; Krzysko, A. J.; Zhang, X.; Hu, J. Z.; Clark, S. B.; Clark, A. E.; Schenter, G. K.; Pearce, C. I.; Rosso, K. M., Al-27 Pulsed Field Gradient, Diffusion-NMR Spectroscopy of Solvation Dynamics and Ion Pairing in Alkaline Aluminate Solutions. *J. Phys. Chem. B* **2018**, *122*, 10907-10912.
- (6) Graham, T. R.; Dembowski, M.; Martinez-Baez, E.; Zhang, X.; Jaegers, N. R.; Hu, J. Z.; Gruszkiewicz, M. S.; Wang, H. W.; Stack, A. G.; Bowden, M. E.; Delegard, C. H.; Schenter, G. K.; Clark, A. E.; Clark, S. B.; Felmy, A. R.; Rosso, K. M.; Pearce, C. I., In Situ Al-27 NMR Spectroscopy of Aluminate in Sodium Hydroxide Solutions above and below Saturation with Respect to Gibbsite. *Inorg. Chem.* **2018**, *57*, 11864-11873.
- (7) Sipos, P.; May, P. M.; Hefter, G., Quantitative Determination of an Aluminate Dimer in Concentrated Alkaline Aluminate Solutions by Raman Spectroscopy. *Dalton Trans.* **2006**, 368-375.
- (8) Johnston, C. T.; Agnew, S. F.; Schoonover, J. R.; Kennedy, J. W.; Page, B.; Osborn, J.; Corbin, R., Raman Study of Aluminum Speciation in Simulated Alkaline Nuclear Waste. *Environ. Sci. Technol* **2002**, *36*, 2451-2458.
- (9) Watling, H., Spectroscopy of Concentrated Sodium Aluminate Solutions. *Appl. Spectrosc.* **1998**, *52*, 250-258.
- (10) Reynolds, J. G.; Reynolds, D. A. A Modern Interpretation of the Barney Diagram for Aluminum Solubility in Tank Waste, Waste Management Symposia Inc., Phoenix, AZ, United States, **2009**
- (11) Wang, H. W.; Graham, T. R.; Mamontov, E.; Page, K.; Stack, A. G.; Pearce, C. I., Counteractions Control Local Specific Bonding Interactions and Nucleation Mechanisms in Concentrated Water-in-Salt Solutions. *J. Phys. Chem. Lett.* **2019**, *10*, 3318-3325.
- (12) Gontijo, G. S.; de Araujo, A. C. B.; Prasad, S.; Vasconcelos, L. G. S.; Alves, J. J. N.; Brito, R. P., Improving the Bayer Process Productivity - An Industrial Case Study. *Miner. Eng.* **2009**, *22*, 1130-1136.
- (13) Den Hond, R.; Hiralal, I.; Rijkeboer, A., Alumina Yield in the Bayer Process Past, Present and Prospects. In *Essential Readings in Light Metals: Volume 1 Alumina and Bauxite*, Donaldson, D.; Raahauge, B. E., Eds. Springer International Publishing: Cham, 2016; pp 528-533.
- (14) Buvári-Barcza, A.; Rozsahegyi, M.; Barcza, L., Hydrogen Bonded Associates in the Bayer Process (In Concentrated Aluminate Lyes): The Mechanism of Gibbsite Nucleation. *J. Mater. Chem.* **1998**, *8*, 451-455.

- (15) Gerson, A. R.; Ralston, J.; Smart, R. S., An Investigation of the Mechanism of Gibbsite Nucleation Using Molecular Modelling. *Colloids Surf. A* **1996**, *110*, 105-117.
- (16) Reynolds, J. G.; McCoskey, J. K.; Herting, D. L., Gibbsite Solubility in Hanford Nuclear Waste Approached from Above and Below Saturation. *Ind. Eng. Chem. Res.* **2016**, *55*, 5465-5473.
- (17) *Report to the Secretary of Energy*; Blue Ribbon Commission on America's Nuclear Future: January 26, 2012.
- (18) Sipos, P., The Structure of Al(III) in Strongly Alkaline Aluminate Solutions - A Review. *J. Mol. Liq.* **2009**, *146*, 1-14.
- (19) Pouvreau, M.; Dembowski, M.; Clark, S. B.; Reynolds, J. G.; Rosso, K. M.; Schenter, G. K.; Pearce, C. I.; Clark, A. E., Ab Initio Molecular Dynamics Reveal Spectroscopic Siblings and Ion Pairing as New Challenges for Elucidating Prenucleation Aluminum Speciation. *J. Phys. Chem. B* **2018**, *122*, 7394-7402.
- (20) Gale, J. D.; Rohl, A. L.; Watling, H. R.; Parkinson, G. M., Theoretical Investigation of the Nature of Aluminum-Containing Species Present in Alkaline Solution. *J. Phys. Chem. B* **1998**, *102*, 10372-10382.
- (21) Bogatko, S.; Geerlings, P., Factors Influencing Al³⁺-Dimer Speciation and Stability From Density Functional Theory Calculations. *Phys. Chem. Chem. Phys.* **2012**, *14*, 8058-8066.
- (22) Sillanpaa, A. J.; Paivarinta, J. T.; Hotokka, M. J.; Rosenholm, J. B.; Laasonen, K. E., A Computational Study of Aluminum Hydroxide Solvation. *J. Phys. Chem. A* **2001**, *105*, 10111-10122.
- (23) Marcus, Y.; Hefter, G., Ion Pairing. *Chem. Rev.* **2006**, *106*, 4585-4621.
- (24) Johansson, G., Crystal Structure of Potassium Aluminate K₂[Al₂O(OH)₆]. *Acta. Chem. Scand.* **1966**, *20*, 505-515.
- (25) Du, C. H.; Zheng, S.; Zhang, Y., Phase Equilibria in the K₂O-Al₂O₃-H₂O System at 40 degrees C. *Fluid Ph. Equilibria* **2005**, *238*, 239-241.
- (26) Busca, G., Catalytic Materials Based on Silica and Alumina: Structural Features and Generation of Surface Acidity. *Prog. Mater. Sci.* **2019**, *104*, 215-249.
- (27) Xu, J.; Wang, Q.; Deng, F., Metal Active Sites and Their Catalytic Functions in Zeolites: Insights from Solid-State NMR Spectroscopy. *Acc. Chem. Res.* **2019**, *52*, 2179-2189.
- (28) Krause, L.; Herbst-Irmer, R.; Stalke, D., An Empirical Correction for the Influence of Low-Energy Contamination. *J. Appl. Crystallogr* **2015**, *48*, 1907-1913.
- (29) Sheldrick, G. M., Crystal Structure Refinement with SHELXL. *Acta Crystallogr C* **2015**, *71*, 3-8.
- (30) Sheldrick, G. M., SHELXT - Integrated Space-Group and Crystal-Structure Determination. *Acta Crystallogr A* **2015**, *71*, 3-8.
- (31) Ildefonse, P.; Cabaret, D.; Sainctavit, P.; Calas, G.; Flank, A. M.; Lagarde, P., Aluminium X-ray absorption near edge structure in model compounds and Earth's surface minerals. *Phys Chem Miner* **1998**, *25* (2), 112-121.
- (32) Ravel, B.; Newville, M., ATHENA, ARTEMIS, HEPHAESTUS: Data Analysis for X-ray Absorption Spectroscopy Using IFEFFIT. *J. Synchrotron Radiat.* **2005**, *12*, 537-541.
- (33) VandeVondele, J.; Krack, M.; Mohamed, F.; Parrinello, M.; Chassaing, T.; Hutter, J., QUICKSTEP: Fast and Accurate Density Functional Calculations Using a Mixed Gaussian and Plane Waves Approach. *Comput. Phys. Commun* **2005**, *167*, 103-128.

- (34) Hammer, B.; Hansen, L. B.; Norskov, J. K., Improved Adsorption Energetics Within Density-Functional Theory Using Revised Perdew-Burke-Ernzerhof Functionals. *Phys. Rev. B* **1999**, *59*, 7413-7421.
- (35) Grimme, S.; Antony, J.; Ehrlich, S.; Krieg, H., A consistent and accurate ab initio parametrization of density functional dispersion correction (DFT-D) for the 94 elements H-Pu. *J Chem Phys* **2010**, *132* (15).
- (36) VandeVondele, J.; Hutter, J., Gaussian Basis Sets for Accurate Calculations on Molecular Systems in gas and Condensed Phases. *J. Chem. Phys* **2007**, *127*, 1-9.
- (37) Ivlieva, V. I.; Ivanov-Emin, B. N.; Kaziev, G. Z.; Gerasimova, T. Y., X-Ray Diffraction Investigation of Rubidium Hydroxoaluminate and Hydroxogallate. *Zh. Neorg. Khim.* **1980**, *25*, 1107.
- (38) van Bokhoven, J. A.; van der Eerden, A. M. J.; Koningsberger, D. C., Three-Coordinate Aluminum in Zeolites Observed with in situ X-ray Absorption Near-Edge Spectroscopy at the Al K-edge: Flexibility of Aluminum Coordinations in Zeolites. *J. Am. Chem. Soc.* **2003**, *125*, 7435-7442.
- (39) Vjunov, A.; Fulton, J. L.; Huthwelker, T.; Pin, S.; Mei, D. H.; Schenter, G. K.; Govind, N.; Camaioni, D. M.; Hu, J. Z.; Lercher, J. A., Quantitatively Probing the Al Distribution in Zeolites. *J. Am. Chem. Soc.* **2014**, *136*, 8296-8306.
- (40) Bove, L. E.; Gaal, R.; Raza, Z.; Ludl, A. A.; Klotz, S.; Saitta, A. M.; Goncharov, A. F.; Gillet, P., Effect of Salt on the H-bond Symmetrization in Ice. *PNAS USA* **2015**, *112*, 8216-8220.
- (41) Cleland, W. W., Low-Barrier Hydrogen Bonds and Enzymatic Catalysis. *Arch. Biochem. Biophys.* **2000**, *382*, 1-5.
- (42) Agmon, N.; Bakker, H. J.; Campen, R. K.; Henchman, R. H.; Pohl, P.; Roke, S.; Thamer, M.; Hassanali, A., Protons and Hydroxide Ions in Aqueous Systems. *Chem. Rev.* **2016**, *116*, 7642-7672.
- (43) Drewitt, M. J.; Niedermann, M.; Baird, M. C., Crystal Structure of the Strongly Hydrogen Bonded Complex Anion $[(C_6F_5)_3B(H_3O_2)B(C_6F_5)_3]^-$. *Inorganica Chim. Acta* **2002**, *340*, 207-210.
- (44) Burguete, M. I.; Escuder, B.; Garcia-Espana, E.; Latorre, J.; Luis, S. V.; Ramirez, J. A., New Strategies in the Development of Polynuclear Complexes. Crystal Structure of the Tetranuclear Copper(II) Complex $[Cu_4(L1)_2(OH)_4Cl_2(H_2O)_2]_2(H_3O_2)(ClO_4)_2Cl \cdot 2H_2O$ (L1=2,5,8,11-tetraaza[12](1,4)naphthalenecyclophane). *Inorganica Chim. Acta* **2000**, *300*, 970-977.
- (45) Bino, A.; Gibson, D., The Hydrogen Oxide Bridging Ligand ($H_3O_2^-$) .1. Dimerization and Polymerization of Hydrolyzed Trinuclear Metal Cluster Ions. *J. Am. Chem. Soc.* **1982**, *104*, 4383-4388.
- (46) Abu-Dari, K.; Raymond, K. N.; Freyberg, D. P., The Bihydroxide ($H_3O_2^-$) Anion. A Very Short, Symmetric Hydrogen Bond. *J. Am. Chem. Soc.* **1979**, *101*, 3688-3689.
- (47) Bino, A.; Gibson, D., A New Bridging Ligand, the Hydrogen Oxide Ion ($H_3O_2^-$). *J. Am. Chem. Soc.* **1981**, *103*, 6741-6742.
- (48) Demunno, G.; Viterbo, D.; Caneschi, A.; Lloret, F.; Julve, M., A Giant Antiferromagnetic Interaction Through the Bihydroxide Bridge ($H_3O_2^-$). *Inorg. Chem.* **1994**, *33*, 1585-1586.
- (49) Winter, J. K.; Ghose, S., Thermal-Expansion and High-Temperature Crystal-Chemistry of the Al_2SiO_5 Polymorphs. *Am. Mineral.* **1979**, *64*, 573-586.

- (50) Krickl, R.; Wildner, M., Crystal Chemistry of Synthetic Co- and Ni-Analogues of Natrochalcite - The Shortest Known Hydrogen Bonds Among Mineral-Type Compounds Part I: Single-Crystal X-ray Structures. *Eur. J. Mineral* **2007**, *19*, 805-816.
- (51) Avvaru, B. S.; Kim, C. U.; Sippel, K. H.; Gruner, S. M.; Agbandje-McKenna, M.; Silverman, D. N.; McKenna, R., A Short, Strong Hydrogen Bond in the Active Site of Human Carbonic Anhydrase II. *Biochemistry* **2010**, *49*, 249-251.
- (52) Puerta, D. T.; Cohen, S. M., [(Tp^{Me,Ph})₂Zn₂(H₃O₂)]ClO₄: A New H₃O₂ Species Relevant to Zinc Proteinases. *Inorganica Chim. Acta* **2002**, *337*, 459-462.
- (53) Yoshimura, Y.; Stewart, S. T.; Somayazulu, M.; Mao, H.; Hemley, R. J., High-Pressure X-ray Diffraction and Raman Spectroscopy of Ice VIII. *J. Chem. Phys.* **2006**, *124*, 1-7.
- (54) Thoeny, A. V.; Gasser, T. M.; Loerting, T., Distinguishing Ice beta-XV from Deep Glassy Ice VI: Raman Spectroscopy. *Phys. Chem. Chem. Phys.* **2019**, *21*, 15452-15462.
- (55) Roberts, S. T.; Petersen, P. B.; Ramasesha, K.; Tokmakoff, A.; Ufimtsev, I. S.; Martinez, T. J., Observation of a Zundel-Like Transition State During Proton Transfer in Aqueous Hydroxide Solutions. *PNAS USA* **2009**, *106*, 15154-15159.
- (56) Chandran, C. V.; Kirschhock, C. E. A.; Radhakrishnan, S.; Taulelle, F.; Martens, J. A.; Breynaert, E., Alumina: Discriminative Analysis Using 3D Correlation of Solid-State NMR Parameters. *Chem. Soc. Rev.* **2019**, *48*, 134-156.
- (57) Casey, W. H., Large Aqueous Aluminum Hydroxide Molecules. *Chem. Rev.* **2006**, *106*, 1-16.
- (58) Weinberger, M.; Schneider, M.; Müller, D.; Geßner, W.; Reck, G., Zur Kenntnis des Natrium-tetrahydroxoaluminat-chlorids Na₂[Al(OH)₄]Cl. *Z. Anorg. Allg. Chem.* **1994**, *620*, 771-776.
- (59) Sipos, P.; Hefter, G.; May, P. M., Al-27 NMR and Raman Spectroscopic Studies of Alkaline Aluminate Solutions with Extremely High Caustic Content - Does the Octahedral Species Al(OH)₆³⁻ Exist in Solution? *Talanta* **2006**, *70*, 761-765.
- (60) Dec, S. F.; Maciel, G. E.; Fitzgerald, J. J., Solid-State Na-23 and Al-27 MAS NMR-Study of the Dehydration of Na₂O-Al₂O₃-3H₂O. *J. Am. Chem. Soc.* **1990**, *112*, 9069-9077.
- (61) Phillips, B. L.; Ohlin, C. A.; Vaughn, J.; Woerner, W.; Smart, S.; Subramanyam, R.; Pang, L., Solid-State Al-27 NMR Spectroscopy of the Gamma-Al-13 Keggin Containing Al Coordinated by a Terminal Hydroxyl Ligand. *Inorg. Chem.* **2016**, *55*, 12270-12280.
- (62) Vjunov, A.; Derewinski, M. A.; Fulton, J. L.; Camaioni, D. M.; Lercher, J. A., Impact of Zeolite Aging in Hot Liquid Water on Activity for Acid-Catalyzed Dehydration of Alcohols. *J. Am. Chem. Soc.* **2015**, *137*, 10374-10382.
- (63) van Bokhoven, J. A.; Sambe, H.; Ramaker, D. E.; Koningsberger, D. C., Al K-edge Near-Edge X-ray Absorption Fine Structure (NEXAFS) Study on the Coordination Structure of Aluminum in Minerals and Y Zeolites. *J. Phys. Chem. B* **1999**, *103*, 7557-7564.
- (64) van Bokhoven, J. A.; Roelofs, J. C. A. A.; de Jong, K. P.; Koningsberger, D. C., Unique Structural Properties of the Mg-Al Hydrotalcite Solid Base Catalyst: An in Situ Study Using Mg and Al K-edge XAFS During Calcination and Rehydration. *Chem-Eur J.* **2001**, *7*, 1258-1265.
- (65) Drake, I. J.; Zhang, Y. H.; Gilles, M. K.; Liu, C. N. T.; Nachimuthu, P.; Perera, R. C. C.; Wakita, H.; Bell, A. T., An in situ Al K-edge XAS Investigation of the Local Environment of H⁺ and Cu⁺ Exchanged USY and ZSM-5 Zeolites. *J. Phys. Chem. B* **2006**, *110*, 11665-11676.

(66) Fulton, J. L.; Govind, N.; Huthwelker, T.; Bylaska, E. J.; Vjunov, A.; Pin, S.; Smurthwaite, T. D., Electronic and Chemical State of Aluminum from the Single- (K) and Double-Electron Excitation (KLII&III, KLI) X-ray Absorption Near-Edge Spectra of alpha-Alumina, Sodium Aluminate, Aqueous $\text{Al}(\text{H}_2\text{O})_6^{3+}$, and Aqueous $\text{Al}(\text{OH})_4^-$. *J. Phys. Chem. B* **2015**, *119*, 8380-8388.

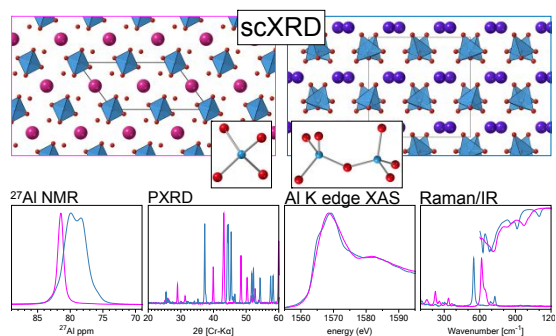
(67) Rehr, J. J.; Kas, J. J.; Vila, F. D.; Prange, M. P.; Jorissen, K., Parameter-Free Calculations of X-ray Spectra with FEFF9. *Phys. Chem. Chem. Phys.* **2010**, *12*, 5503-5513.

(68) Goryainov, S. V., A Model of Phase Transitions in Double-Well Morse Potential: Application to Hydrogen Bond. *Physica B* **2012**, *407*, 4233-4237.

(69) Davydov, A. S., The Theory of Molecular Excitons. *Soviet Physics Uspekhi* **1964**, *7*, 145-178.

(70) Shi, L.; Gruenbaum, S. M.; Skinner, J. L., Interpretation of IR and Raman Line Shapes for H_2O and D_2O Ice Ih. *J. Phys. Chem. B* **2012**, *116*, 13821-13830.

(71) Vacque, V.; Sombret, B.; Huvenne, J. P.; Legrand, P.; Suc, S., Characterisation of the O-O Peroxide Bond by Vibrational Spectroscopy. *Spectrochim. Acta A* **1997**, *53*, 55-66.



Tetrahedrally coordinated Al(OH)₄⁻ and Al₂O(OH)₆²⁻ have been isolated in the solid-state and interrogated using XRD, NMR, XAS, IR, and Raman.